ADVANCED ENGINEERING MATERIALS
www.aem-journal.com

Nanoengineering Approaches to Tune Thermal and Electrical Conductivity of a BiSbTe Thermoelectric Alloy

*Saeed Masoumi and Amir Pakdel**

Nanoengineering of thermoelectric (TE) materials is an effective approach to decouple their electronic and thermal transport properties, hence enhancing their TE efficiency. Nanoengineering strategies can significantly reduce the thermal conductivity through the corporation of different phonon scattering mechanisms, whereas the electrical conductivity may not be affected considerably. Herein, the effects of three nanoengineering approaches on the structural, electrical, and thermal properties of $Bi_{0.5}Sb_{1.5}Te_3$ (BST) alloy are compared: (a) nanohybridization of the alloy by adding Sb_2O_3 nanoparticles, (b) severe plastic deformation via high-pressure torsion, and (c) grain refinement by sonication of BST powders before sintering. It is shown that among these methods, severe plastic deformation induces ultrafine grains and a high density of dislocations, resulting in a large reduction of the total thermal conductivity (32.8%) and a moderate decline in the electrical conductivity of (15.7%) at 300 K. A notable decrease in the lattice thermal conductivity (56.8% at 300 K) is attributed to midfrequency phonon scattering by the dislocations together with low and high frequency scatterings through grain boundaries and point defects, respectively. A new pathway is opened for designing highly efficient TE materials through nanoengineering approaches, particularly severe plastic deformation.

1. Introduction

Greenhouse gas emission is the major cause of climate change and global warming.[1–3] Major advancements have been made in science and technology to harvest, convert, and store different forms of energy, which have provided breakthroughs in reducing the greenhouse gases.[4–8] We know that a significant amount of waste heat is produced every day in various sectors such as transportation, buildings, conventional power plants, and different branches of industry. Therefore, efficient harvesting and usage of waste heat is an effective way to improve the sustainability of energy sources and to reduce the emission of greenhouse gases.[9,10] Thermoelectric (TE) materials and devices are capable of directly converting waste heat into electricity, thus a desirable solution to efficiently reduce energy consumption and improve energy management.[11–13] A measure to evaluate the quality of TE materials for converting heat into electricity is the dimensionless figure of merit $ZT = S^2\sigma T/K$, where S is the Seebeck coefficient, σ is the electrical conductivity, K is the thermal conductivity, and T is the absolute temperature.[14–16] Transport of charge carriers and phonons determines the thermal and electrical properties of a TE material, thus its TE efficiency. To demonstrate a high ZT value, a TE material needs to have a large Seebeck coefficient, high electrical conductivity, and low thermal conductivity. However, these fundamental transports properties are inter-related. To decouple and optimize these properties, a paradigm shift from bulk and conventional TE materials toward novel nanomaterials, heterostructures, and nanocomposites has taken place in the past two decades.[17–19] Using low-dimensional TE materials and composites not only decreases the thermal conductivity via enhanced phonon scattering at the interfaces, but it may also increase the Seebeck coefficient by energy filtering of charge carriers at the interfacial potential barriers.[20–22]

BiSbTe alloys are among the best p-type TE material systems with peak ZT values in the range of 0.8–1.1 near room temperature.[23–25] Therefore, recent methodologies for nanostructuring and nanoengineering of these alloys have stimulated a new wave of interest in the field of thermoelectricity. In this regard, most research articles have focused on preparation of bulk nanostructured TE materials by: (1) sintering TE nanoparticles into bulk samples, (2) in situ precipitation of a nanophase in a bulk sample, and (3) chemical reactions to produce nanocomposite TE samples.[26,27] Moreover, severe plastic deformation (SPD) and sonication have been utilized to produce ultrafine grains and a higher concentration of structural defects, e.g., grain boundaries, vacancies, and dislocations, to reduce the thermal conductivity and increase the Seebeck coefficient.[28–31] However, the SPD method has been used mostly in skutterudites, half-Heusler, and lead telluride alloys, and sonication methods have been mostly applied to oxide-based TE materials and organic/inorganic nanocomposites. There are limited reports on the production of nanostructured BiSbTe alloys by SPD or sonication

S. Masoumi, A. Pakdel
Department of Mechanical, Manufacturing & Biomedical Engineering
Trinity College Dublin
The University of Dublin
Dublin D02PN40, Ireland
E-mail: pakdela@tcd.ie

The ORCID identification number(s) for the author(s) of this article can be found under https://doi.org/10.1002/adem.202100955.

DOI: 10.1002/adem.202100955

techniques.[32] Here, for the first time, we have investigated the effect of SPD, sonication, and nanohybridization on structural, electrical, and thermal properties of a nominal $Bi_{0.5}Sb_{1.5}Te_3$ (from now on referred to as BST) composition. The results revealed that the electrical conductivity in all these three types of samples was smaller than that of the reference sample due to attenuation of charge carrier transport by structural defects. Furthermore, the SPD process led to a significant reduction of lattice thermal conductivity due to intensive increase in the mid-frequency phonon scattering at dislocation arrays.

2. Results and Discussion

2.1. Microstructure and Chemical Composition

Figure 1a shows a scanning electron microscope (SEM) image of milled BST powder with a wide range of particle sizes, mostly hundreds of nm to several μm. The corresponding energy-dispersive spectroscopy (EDS) analysis in Figure 1b displays peaks of Bi, Sb, and Te at atomic weight percent ratios of 10.1%, 31.1%, and 59.8%, respectively. This confirms the stoichiometric composition of the BST product after sintering. The extra peaks in Figure 1b are related to C, Al, and Be, generated from the substrate (carbon tape), sample holder, and EDS detector, respectively. Figure 1c shows the XRD pattern of the BST alloy after spark plasma sintering (SPS) process. All peaks are indexed to Bi–Sb–Te phase (COD#1 530 822, PDF#721 836, and JCPDS#49-1713), with an R-3m rhombohedral structure.

Figure 1d shows an SEM image of the BST powder after tip sonication. It can be noticed that the average powder size has decreased dramatically as compared with Figure 1a. The majority of the particles are in the size range of tens to hundreds of nanometers. The tip sonication process led to particle fragmentation and downsizing but did not yield ultrathin platelets as we had expected. In fact, the sonication energy in this process induces vibrations that can result in: 1) creation of large shear forces that separate powders apart and peel off individual thin layers by overcoming the binding energy between the material layers, and 2) creation and collapse of microbubbles that can form microjets and shockwaves, which facilitate debundling to obtain finer exfoliated layers.[33] In our experiments, however, the inflow of sonication energy resulted largely in particle fracture and much less in exfoliation of atomic layers. We also experimented sonication of BST powders in isopropyl alcohol (IPA) and *N*-methyl-2-pyrrolidone (NMP) to test if solvents with different polarities and surface tension may yield different results, but the final outcome in all the cases was fragmented nanoparticles rather than thin 2D platelets.

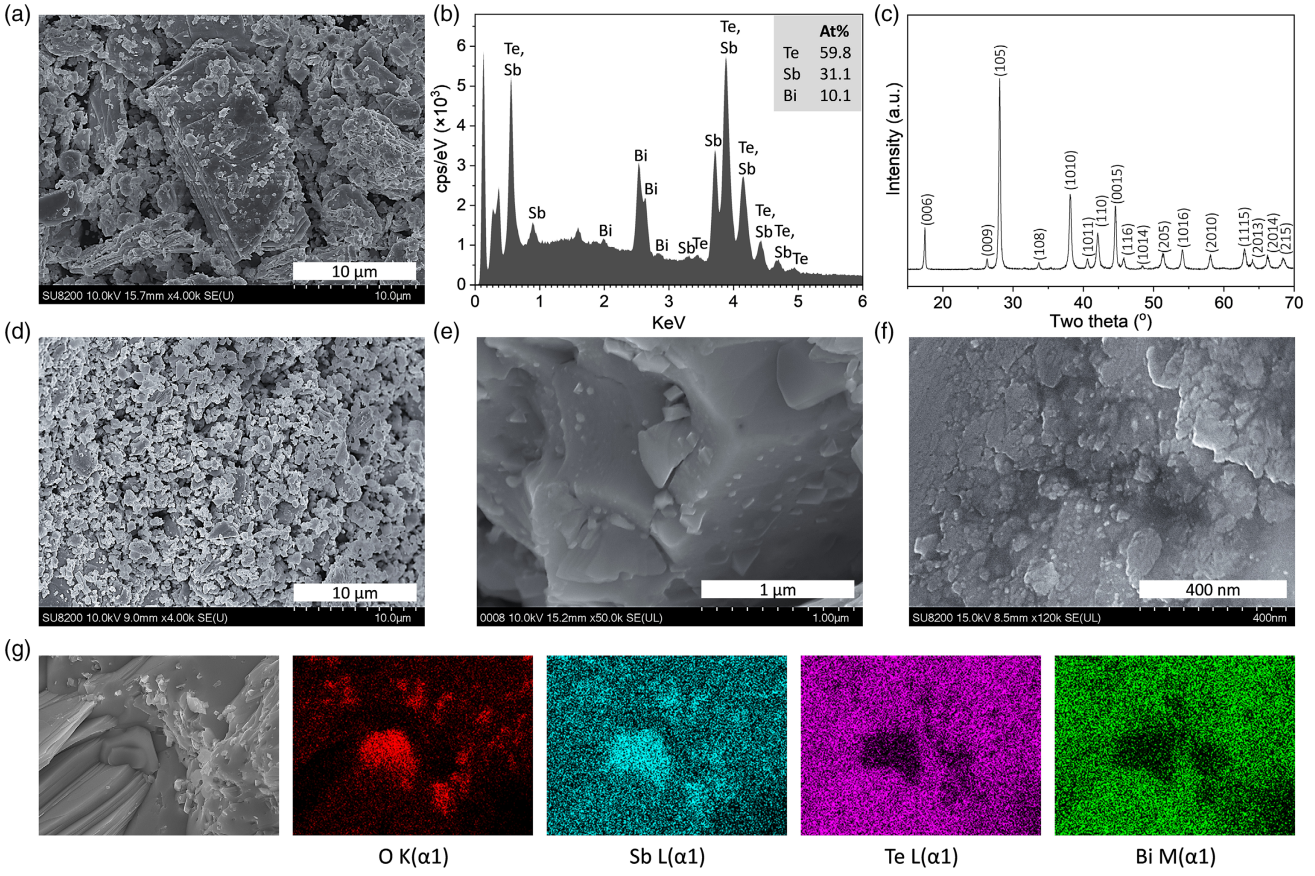

Figure 1. a) SEM image and b) EDS analysis of reference BST powder, c) XRD patterns of reference BST sample after SPS process, SEM images of d) a BST powder after tip sonication, e) a BST/Sb_2O_3 nanocomposite sample after sintering, and f) the fracture surface of a BST sample after HPT processing. g) EDS elemental mapping of a BST/Sb_2O_3 sample.

Figure 1e shows an SEM image of a BST/Sb_2O_3 nanocomposite after sintering. A small piece was cut from the sintered disc for this cross-sectional examination. It is evident that the nanoparticles are distributed throughout the BST grains and into the grain boundaries. Figure 1g shows representative EDS elemental maps of the nanocomposite confirming the distribution of antimony oxide particles in the BST matrix. Figure 1f shows the fracture surface of a BST sample after high-pressure torsion (HPT) processing. It is noticed that the grain size reduced greatly due to the severe plastic deformation applied at room temperature. During the HPT process, surface frictional forces deform the disc by shear and large deformations occur under a quasihydrostatic pressure.[34] As a result, the deformed regions may demonstrate a combination of ultrafine grains and a high density of dislocations together with recrystallized regions almost free of dislocations.[35] This can be seen in the bright-field and dark-filed scanning transmission electron microscope (STEM) images in **Figure 2**a,b. A large concentration of dislocations on the right side of the sample is distinguishable from the almost dislocation-free left side. Despite the large deformation that the BST alloy underwent during the HPT process, the high-resolution TEM image in Figure 2c shows a high level of crystallinity in the sample.

2.2. Physical Properties

The temperature dependence of electrical conductivity is shown in **Figure 3**a, where σ decreased with temperature in all samples. This trend implies that the samples behave as degenerate semiconductors, similar to metals. The pristine BST demonstrated higher electrical conductivity than the nanoengineered samples. The SPD sample had lower electrical conductivity than the reference BST and showed a 15.7% decline at room temperature. Similarly, the sonicated and nanocomposite samples showed smaller electrical conductivity values of ≈6.2% and ≈9.5%, respectively, in comparison with the reference BST. The reduction of electrical conductivity in the deformed and sonicated samples was mainly due to multiplication of structural dislocations and grain boundaries in their microstructures, respectively. The established energy barriers at dislocations and grain boundaries can attenuate the charge carrier transport, hence decrease the electrical conductivity. This is further supported by the recent literature on sever plastic deformation of TE materials, where negligible changes in the charge carrier concentration of the samples were observed after the SPD process.[29,31,36] However, future analysis is required to analyze the potential formation of antisite defects during plastic deformation and consequential increase in the charge carrier concentration in BiSbTe alloys. In case of the nanocomposite sample, in addition to charge carrier scattering by Sb_2O_3 nanoparticles, a decrease in effective charge carrier concentration was also witnessed, which further contributed to the reduction of electrical conductivity. In fact, the charge carrier concentration of BST/4 wt% Sb_2O_3 was 2.2×10^{25} ($1/m^3$), 37.1% smaller than that of the pristine BST (3.5×10^{25} [$1/m^3$]).[21]

The variation of thermal transport properties with temperature in all samples is shown in Figure 3b–d. As shown in Figure 3b, K_{tot} of the reference BST, sonicated, and nanocomposite samples moderately declined with temperature, and after reaching a minimum value, it increased. This behavior is attributed to the bipolar effect caused by the generation of electron–hole pairs at higher temperatures through the excitation process across the bandgap.[22,32] Moreover, effective bipolar effect occurred at higher temperatures in nanocomposite and sonicated samples in comparison with the pristine BST sample. Conversely, the total thermal conductivity gradually raised with temperature in the SPD sample. This trend has also been observed in some half-Heusler alloys and skutterudite systems, such as $Ti_{0.5}Zr_{0.5}NiSn$,[31] $DD_yFe_3CoSb_{12}$,[28] and $(Mm, Sm)_yCo_4Sb_{12}$.[29] This type of temperature dependency of K_{tot} can be attributed to changes in the density and rearrangement of dislocations in the SPD samples, during the early stages of heating.

The sonicated and nanocomposite samples demonstrated 3.6−11.6% reductions in K_{tot} in comparison with the reference BST sample at 300−425 K. The SPD sample showed a more significant decrease of 26.3−32.8% in K_{tot} at this temperature range as compared with the reference BST sample. The total thermal conductivity comprises two components: electronic thermal conductivity and lattice thermal conductivity. The calculated electronic thermal conductivities in Figure 3c show that nanocompositing, grain refinement by sonication, and severe plastic deformation reduced the electronic thermal conductivity due to carrier scattering by the established energy barriers at the BST/Sb_2O_3 interfaces, grain boundaries, and dislocations in their microstructures, respectively. The charge carrier scattering

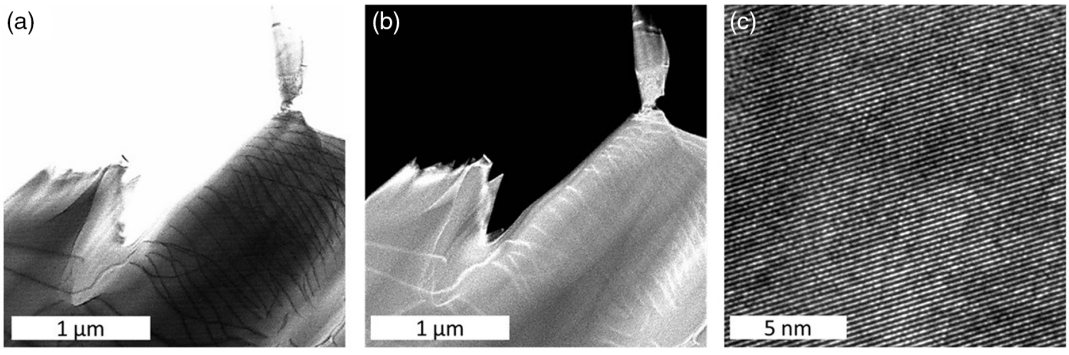

Figure 2. a) The bright-field, b) dark-filed STEM images, and c) the high-resolution TEM image of BST sample after HPT process.

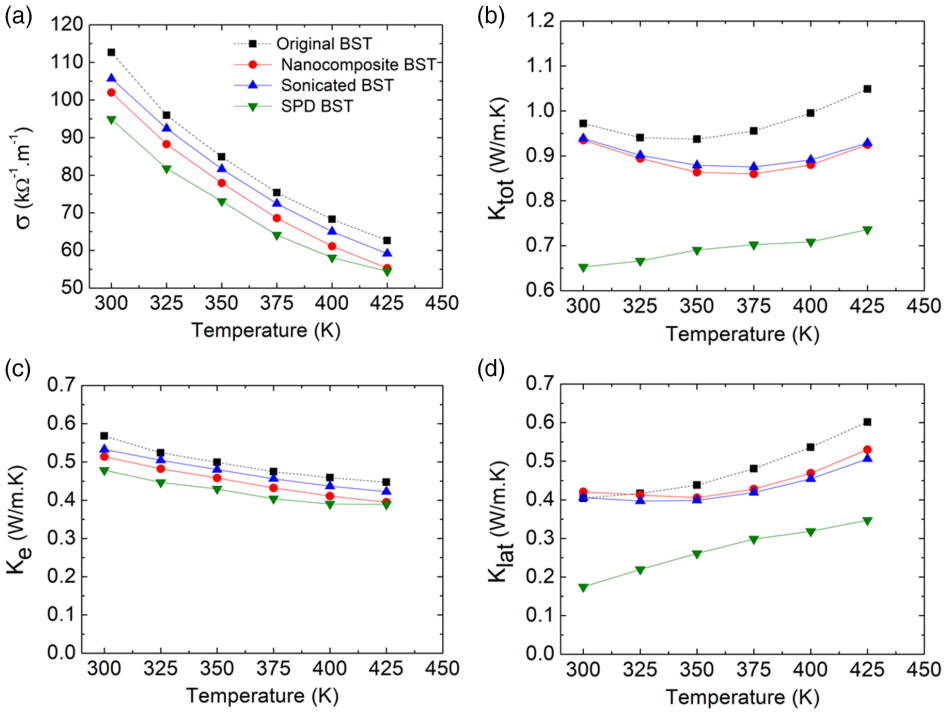

Figure 3. Temperature dependence of a) electrical conductivity, b) total thermal conductivity, c) electronic thermal conductivity, and d) lattice thermal conductivity in reference BST, nanocomposite, sonicated, and sever plastic deformed samples.

effect is intensified at higher temperatures; thus, K_e decreases with temperature in all samples. The lattice thermal conductivities, in contrast, depicted an opposite trend of variation with temperature in all samples (Figure 3d). In general, the lattice thermal conductivity of the reference BST sample was larger than those of sonicated and nanocomposite samples at $\geq$325 K, and the differences became more noticeable at higher temperatures. Moreover, the severe plastic deformation significantly decreased K_{lat} in the whole temperature range. There was a maximum reduction of 56.8% in K_{lat} of the SPD sample compared with the reference BST sample at 300 K. The reduction of lattice thermal conductivity in the samples can be attributed to phonon scattering by the BST/Sb_2O_3 interfaces, grain boundaries, and dislocations engineered in the microstructures. Furthermore, comparing the lattice and electronic thermal conductivities, the phonon scattering effect was more prominent than electron scattering in all nanoengineered samples. Particularly, the significant decline of the total thermal conductivity in the SPD sample is attributed to the large reduction of the lattice thermal conductivity due to the presence of a high density of dislocations.

The phonons that carry the heat energy in a crystal cover a wide range of frequency (ϑ). The lattice thermal conductivity is defined as the integration of different contributions at various frequencies[22,37]

$$K_{lat} = \int K_s(\vartheta) d\vartheta \tag{1}$$

where $K_s(\vartheta)$ is the spectral lattice thermal conductivity which can be expressed as

$$K_s(\vartheta) = C_p(\vartheta) \times V^2(\vartheta) \times \tau(\vartheta) \tag{2}$$

in which, $C_p(\vartheta)$ is the spectrum of phonon heat capacity, $V(\vartheta)$ is the spectrum of phonon velocity, and $\tau(\vartheta)$ is the spectrum of phonon scattering time.[38] In a low-defect crystalline sample, the phonons are scattered by Umklapp scattering. In this scattering mechanism, by considering a $\tau_U^{-1}(\vartheta) \sim \vartheta^2$ and $C_p(\vartheta) = \vartheta^2$, the $K_s(\vartheta)$ becomes almost constant which results in the contribution of phonons with a broad range of frequencies to thermal conductivity.[38] However, the lattice thermal conductivity in polycrystalline materials is also affected by the scattering of phonons at microstructural defects. High-frequency and low-frequency phonons can be scattered by point defects and grain boundaries, respectively. Further reduction of lattice thermal conductivity can be obtained by incorporation of dislocations in the microstructure as they contribute to midfrequency phonon scattering. That is, the dislocation scattering mechanisms target the phonons with the midrange frequency which are not scattered by other mechanisms. The combination of different scattering mechanisms including point defects, grain boundaries, and dislocations can provide a platform for maximizing the reduction of lattice thermal conductivity through scattering of a full spectrum of phonons from low to high frequencies.

The microstructures and scattering mechanisms of all four types of samples are schematically shown in **Figure 4**a–d. As shown in Figure 4a for the pristine BST sample with a wide range of grain sizes, the low- and high-frequency phonons are mainly scattered through the Umklapp, point defect, and grain boundary scattering mechanisms. In this sample, the point defects are the local Bi–Sb–Te disorders in the microstructure.[22] Figure 4b

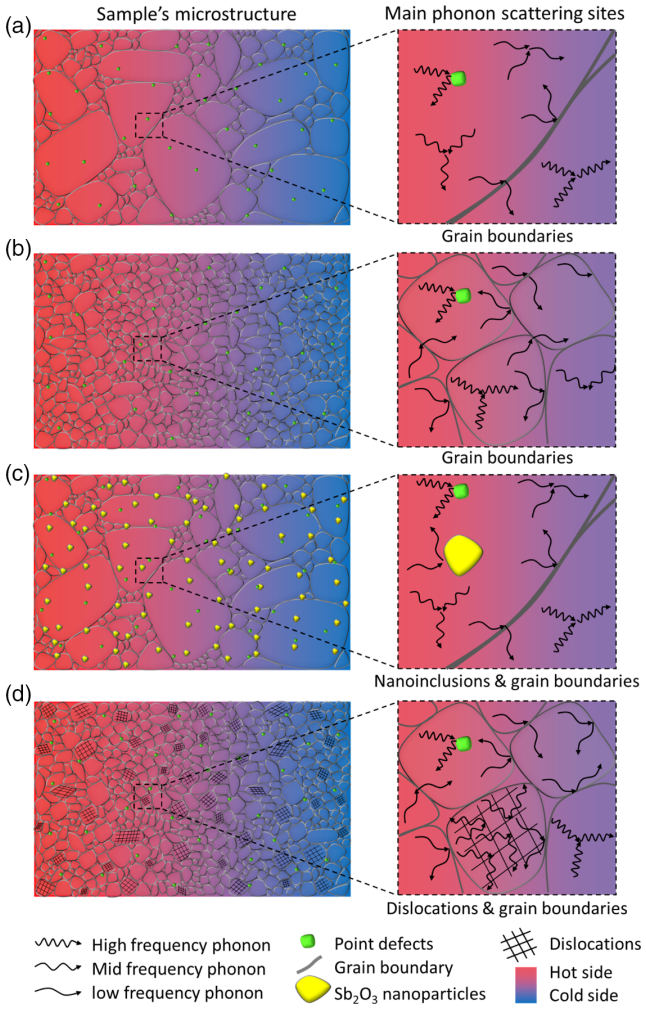

Figure 4. The schematic presentation of the microstructures and different scattering mechanisms in a) reference BST, b) sonicated BST, c) BST/Sb_2O_3 nanocomposite, and d) severely plastic deformed BST. The major scattering mechanism(s) are identified in each panel. (a) Grain boundary scattering as the dominant mechanism in pristine BST is shown. (b) Enhanced grain boundary scattering due to the presence of nanosized grains in sonicated BST is shown. (c) Scattering from nano-oxide particles as the major scattering mechanism in BST nanocomposites is shown. (d) Ultrafine grain boundaries and dislocation arrays are the dominant scattering mechanisms in the severely deformed BST sample.

shows the microstructure and scattering mechanism in the sonicated BST sample. The nanograins and large number of grain boundaries in this sample contribute to enhanced scattering of low frequency phonons. In contrast, the addition of Sb_2O_3 nanoparticles to the BST matrix in Figure 4c decreases the lattice thermal conductivity through incorporation of low-frequency phonon scattering mechanisms. Finally, the SPD sample not only contains ultrafine grains and large number of grain boundaries but also a high density of dislocations. As schematically shown in Figure 4d, in addition to the aforementioned scattering mechanisms, dislocation arrays can effectively scatter the midfrequency phonons. This can provide a full spectrum of phonon scattering in low- to high-frequency ranges, as evidenced by the significant decrease in the lattice thermal conductivity of the SPD sample.

3. Conclusion

The effect of three nanoengineering approaches on the structural, electrical, and thermal properties of a BST alloy was investigated. Sb_2O_3 nanoparticles addition to the alloy, grain refinement by sonication, and generation of high density of dislocations by SPD resulted in reduction of both thermal and electrical conductivity, as compared with the pristine BST sample. Such nanoengineering approaches can enhance the overall TE performance of inorganic semiconductors; for instance, the ultrafine grain size and compact dislocation substructure in the severely deformed BST sample resulted in a substantial 32.8% decrease in total thermal conductivity but a moderate 15.7% reduction in electrical conductivity at 300 K.

4. Experimental Section

Synthesis and Thermomechanical Processing: A nominal composition of BST was selected for the pure alloy. Stochiometric quantities of Bi (−100 mesh, ≥99.99%, Sigma Aldrich), Sb (−100 mesh, 99.5%, Sigma Aldrich), and Te (−200 mesh, >99.8%, Sigma Aldrich) powders were mixed and sealed in an evacuated quartz ampule. The ampule was moved into an electric furnace to melt the mixed powders at 970 K, followed by slow cooling to room temperature during a 48 h time span. The ampule was then broken to remove the solidified alloy, which was later manually grinded using a mortar and a pestle, and finally ball milled. The grinded powder was divided into four equal masses and those portions were ball milled for 0, 30, 120, and 240 min, and finally all mixed together to obtain BST powders with a range of nm to μm sizes. The mixed powder was placed in a graphite die (Φ 10 mm) and spark plasma sintered (SPS-1080 System, SPS SYNTEX Inc.) in an argon atmosphere at 808 K for 5 min under a 46 MPa uniaxial pressure. This yielded dens BST discs.

To achieve severe plastic deformation on the BST discs, a HPT machine (RE-HPT-60-05, Riken Enterprise Co. Ltd.) was used at room temperature. A BST disc was placed between the machine anvils, then the lower anvil moved toward the upper one until a pressure of ≈3 GPa was applied to the sample and held for 5 min. Subsequently, the lower anvil was rotated at a 1 rpm speed relative to the upper anvil, whereas the applied pressure was kept unchanged. This process was terminated after 5 min and the deformed disc was collected from the machine. To manufacture samples with finer grain size, the grinded and milled BST powder was immersed in *N*-cyclohexyl-2-pyrrolidone (CHP). The suspension was sonicated for 60 min using a tapered-probe sonic tip (VibraCell CVX, 750 W) under cooling, yielding a stock dispersion. Aliquots of the stock dispersion were centrifuged at 500 rpm for 12 h (Hettich Mikro 220R). The fine powder was then consolidated by SPS. Finally, to manufacture nanocomposite samples, 4 wt% Sb_2O_3 nanoparticles (<200 nm, >99.9%, Sigma Aldrich) were mixed with milled BST powder and were then consolidated by SPS at 808 K for 5 min under a uniaxial pressure of 46 MPa.

Chemical and Structural Characterization: The characterization of phase composition was performed by powder X-ray diffraction (Rigaku Ultima) with Cu Kα radiation. Microstructural and chemical composition analysis was carried out by a field-emission SEM (SU8200 Hitachi) equipped with an EDS system. Structural analysis was carried out by a field emission transmission electron microscope (JEOL, JEM-2100F) equipped with an annular STEM detector.

Physical Property Measurements: The thermal diffusivity coefficient (D) was measured using a laser flash thermal analyser (ULVAC TC-7000). The heat capacity (C_p) was measured using a differential scanning calorimetry method (DSC, Netzsch STA 449). The density of each sample (ρ) was

calculated using its mass-to-volume ratio. The total thermal conductivity (K_{tot}) was then calculated by the formula $K_{tot} = D.\rho.C_p$. To calculate the electronic thermal conductivity (K_e), the Wiedemann–Franz law ($K_e = \sigma.L.T$) was used. The electronic thermal conductivity was subtracted from the total thermal conductivity to obtain lattice thermal conductivity (K_{lat}). In the absence of Seebeck coefficient values for some samples, the Lorenz number (L) was estimated $1.68 \times 10^{-8}\,W\Omega K^{-2}$ for all samples. The authors' previous works on BST alloys and BST/Sb_2O_3 nanocomposites indicate that the Fermi integral function gives Lorenz numbers of $1.64-1.72 \times 10^{-8}\,W\Omega K^{-2}$ in the temperature range 300−425 K.[21] That is within ±3% of the assumed Lorenz number in this work ($1.68 \times 10^{-8}\,W\Omega K^{-2}$) making it a realistic and acceptable estimation. The sintered discs were cut into rectangular bars for electrical conductivity measurements using a home-made four-probe measurement setup.[39,40]

Acknowledgements

This research was supported by Science Foundation Ireland (SFI), grant no. 18/SIRG/5621. The authors are grateful to Prof. Takao Mori, Prof. Koichi Tsuchiya, and the Transmission Electron Microscopy Station in NIMS (Japan) for discussion and technical support.

Open access funding provided by IReL.

Conflict of Interest

The authors declare no conflict of interest.

Data Availability Statement

Research data are not shared

Keywords

BiSbTe alloys, dislocations, grain refinement, nanoengineering, thermoelectrics

Received: July 27, 2021
Revised: September 7, 2021
Published online: October 1, 2021

[1] D. A. Lashof, D. R. Ahuja, *Nature* **1990**, *344*, 529.
[2] M. Meinshausen, N. Meinshausen, W. Hare, S. C. Raper, K. Frieler, R. Knutti, D. J. Frame, M. R. Allen, *Nature* **2009**, *458*, 1158.
[3] H. Jin, W. Bing, E. Jin, L. Tian, Y. Jiang, *Adv. Mater. Interfaces* **2020**, *7*, 1901577.
[4] X.-L. Shi, J. Zou, Z.-G. Chen, *Chem. Rev.* **2020**, *120*, 7399.
[5] J. Y. Kim, J.-W. Lee, H. S. Jung, H. Shin, N.-G. Park, *Chem. Rev.* **2020**, *120*, 7867.
[6] E. Faegh, B. Ng, D. Hayman, W. E. Mustain, *Nat. Energy* **2021**, *6*, 21.
[7] X. Fan, H. Yang, X. Wang, J. Han, Y. Wu, L. Gou, D. L. Li, Y. L. Ding, *Adv. Mater. Interfaces* **2021**, *8*, 2002184.
[8] W. Zhao, T. Chen, W. Wang, S. Bi, M. Jiang, K. Y. Zhang, S. Liu, W. Huang, Q. Zhao, *Adv. Mater. Interfaces* **2021**, *8*, 2100308.
[9] S.-R. Yan, M. A. Fazilati, N. Samani, H. R. Ghasemi, D. Toghraie, Q. Nguyen, A. Karimipour, *J. Energy Storage* **2020**, *30*, 101445.
[10] S. Bai, C. Liu, *Renewable Sustainable Energy Rev.* **2021**, *147*, 111188.
[11] R. Freer, A. V. Powell, *J. Mater. Chem. C* **2020**, *8*, 441.
[12] A. U. Khan, R. A. R. A. Orabi, A. Pakdel, J.-B. Vaney, B. Fontaine, R. G. Gautier, J.-F. O. Halet, S. Mitani, T. Mori, *Chem. Mater.* **2017**, *29*, 2988.
[13] R. Welch, D. Hobbis, A. J. Birnbaum, G. Nolas, S. LeBlanc, *Adv. Mater. Interfaces* **2021**, *8*, 2100185.
[14] G. Prunet, F. Pawula, G. Fleury, E. Cloutet, A. J. Robinson, G. Hadziioannou, A. Pakdel, *Mater. Today Phys.* **2021**, *18*, 100402.
[15] W. Ding, P. Liu, Z. Bai, Y. Wang, G. Liu, Q. Jiang, F. Jiang, P. Liu, C. Liu, J. Xu, *Adv. Mater. Interfaces* **2020**, *7*, 2001340.
[16] H. J. Cho, Y. Takashima, Y. Nezu, T. Onozato, H. Ohta, *Adv. Mater. Interfaces* **2020**, *7*, 1901816.
[17] G. J. Snyder, E. S. Toberer, Materials for sustainable energy: A collection of peer-reviewed research and review articles from Nature Publishing Group **2011**, p. 101.
[18] J. He, T. M. Tritt, *Science* **2017**, *357*, eaak9997.
[19] Y. J. Wu, Y. W. Lan, S. C. Hsu, C. H. Yeh, Y. S. Ku, J. C. Jiang, Y. Xu, *Adv. Mater. Interfaces* **2020**, *7*, 2000364.
[20] F. Hossein-Babaei, S. Masoumi, A. Noori, *J. Mater. Chem. A* **2018**, *6*, 10370.
[21] A. Pakdel, Q. Guo, V. Nicolosi, T. Mori, *J. Mater. Chem. A* **2018**, *6*, 21341.
[22] S. I. Kim, K. H. Lee, H. A. Mun, H. S. Kim, S. W. Hwang, J. W. Roh, D. J. Yang, W. H. Shin, X. S. Li, Y. H. Lee, *Science* **2015**, *348*, 109.
[23] I. T. Witting, T. C. Chasapis, F. Ricci, M. Peters, N. A. Heinz, G. Hautier, G. J. Snyder, *Adv. Electron. Mater.* **2019**, *5*, 1800904.
[24] J. Mao, G. Chen, Z. Ren, *Nat. Mater.* **2021**, *20*, 454.
[25] B. Huang, G. Li, B. Duan, P. Zhai, W. A. Goddard III, *Scr. Mater.* **2021**, *202*, 114016.
[26] Y. Zheng, T. Zhu, X. Zhao, J. Tu, G. Cao, *Mater. Lett.* **2005**, *59*, 2886.
[27] Z. Liang, M. J. Boland, K. Butrouna, D. R. Strachan, K. R. Graham, *J. Mater. Chem. A* **2017**, *5*, 15891.
[28] G. Rogl, A. Grytsiv, R. Anbalagan, J. Bursik, M. Kerber, E. Schafler, M. Zehetbauer, E. Bauer, P. Rogl, *Acta Mater.* **2018**, *159*, 352.
[29] G. Rogl, K. Yubuta, M. Kerber, A. Grytsiv, M. Zehetbauer, E. Bauer, P. Rogl, *Acta Mater.* **2019**, *173*, 9.
[30] G. Rogl, S. Ghosh, O. Renk, K. Yubuta, A. Grytsiv, E. Schafler, M. Zehetbauer, R. C. Mallik, E. Bauer, P. Rogl, *J. Alloys Compd.* **2021**, *854*, 156678.
[31] G. Rogl, M. J. Zehetbauer, P. F. Rogl, *Mater. Trans.* **2019**, *60*, 2071.
[32] J. A. S. Regueiro, Towards high performance bulk thermoelectric materials with enhanced mechanical properties by Severe Plastic Deformation (SPD), Universidad de Navarra, **2015**.
[33] Z. Baig, O. Mamat, M. Mustapha, A. Mumtaz, K. S. Munir, M. Sarfraz, *Ultrason. Sonochem.* **2018**, *45*, 133.
[34] A. P. Zhilyaev, T. G. Langdon, *Prog. Mater. Sci.* **2008**, *53*, 893.
[35] D. Ahmadkhaniha, Y. Huang, M. Jaskari, A. Järvenpää, M. H. Sohi, C. Zanella, L. P. Karjalainen, T. G. Langdon, *J. Mater. Sci.* **2018**, *53*, 16585.
[36] G. Rogl, S. Ghosh, L. Wang, J. Bursik, A. Grytsiv, M. Kerber, E. Bauer, R. C. Mallik, X.-Q. Chen, M. Zehetbauer, *Acta Mater.* **2020**, *183*, 285.
[37] H. J. Goldsmid, *Electronic Refrigeration*, Pion **1986**.
[38] E. S. Toberer, A. Zevalkink, G. J. Snyder, *J. Mater. Chem.* **2011**, *21*, 15843.
[39] S. Masoumi, A. Noori, M. Shokrani, F. Hossein-Babaei, *IEEE Trans. Instrum. Meas.* **2019**, *69*, 3070.
[40] F. Hossein-Babaei, S. Masoumi, A. Noori, *Meas. Sci. Technol.* **2017**, *28*, 115002.